Polarization-dependent magnetism of the Ni/$BaTiO_3$ interface

A. E. Bocirnea, D. G. Popescu,* C. Chirila, R. M. Costescu, V. Kuncser, V. Stancu, L. Trupina, I. Pasuk, A. M. Vlaicu, and M. A. Husanu

National Institute of Materials Physics, Atomistilor 405a, 077125 Magurele-Ilfov, Romania

(Received 31 July 2019; revised manuscript received 20 January 2020; accepted 29 January 2020; published 4 March 2020)

We explore the cross coupling between the ferroelectric and ferromagnetic phases in Ni/$BaTiO_3$(001) heterostructures and demonstrate the modulation of the magnetism and incidence of exchange bias in the ultrathin metallic Ni overlayer, depending on the ferroelectric state of the bottom layer. We establish that 5-nm-thick monocrystalline Ni film deposited on $BaTiO_3$ with ferroelectric polarization pointing towards the surface (P+) favors the organization of Ni into uniform ferromagnetic domains. Ni grown on $BaTiO_3$ with opposite ferroelectric polarization is featured by emerging exchange-bias coupling between the ferromagnetic Ni top layers and the antiferromagnetic reacted interface, as theoretically explained by first-principles calculations. We explicitly obtain the morphology of the magnetic domains of the crystalline Ni layer in atomic and magnetic force microscopy measurements (AFM/MFM). The resemblance of AFM and MFM images indicate that, although with radically different morphologies, in both cases all spins orient in the Ni plane. Consequently, the distinct signature of the ferroelectric-ferromagnetic coupling extracted from the magneto-optical Kerr effect measurements encodes all the information of sample magnetism. The peculiar magnetic coupling depending on the ferroelectric state indicates new ways of engineering the functionality of metal/ferroelectric interfaces.

DOI: 10.1103/PhysRevMaterials.4.034402

I. INTRODUCTION

Systems combining different ferroic phases are an attractive realm for developing devices with functionality enriched at the interface between dissimilar materials. There is already solid evidence for the coupling of magnetism with ferroelectricity achieved for combinations of metals (Fe [1,2], Co [3]) or oxides with metallic conduction ($LaSrMnO_3$, $LaCaMnO_3$ [4]) at the interface with ferroelectrics ($PbZrTiO_3$−PZT [4], $BaTiO_3$−BTO [1], $Pb(Mg_xNb_{1-x})O_3$−$PbTiO_3$ [5]) or organic ferroelectrics [6]. The transition from metal to an insulating state triggered by switching of the ferroelectric polarization accompanies, for example, changes of the magnetic ground state [ferromagnetic (FM) to antiferromagnetic (AFM)] [7]. The mechanism relies on local alteration of the metal electronic structure near the interface region [4,8], either driving the metal across its phase diagram [7,9] or modulating the chemical bond and overlap of the atomic wave function, changing the orbital population, thus modifying the magnetic component and the double-exchange mechanisms [9–11]. In addition, electric-field modulations of the Dzyaloshinskii-Moriya interaction and Rashba effect at artificial multiferroic interfaces opens the way to manipulating topological magnetic phases [5,12–14].

A conceptual case, particularly simple to put in practice, is the metal adlayer on ferroelectric surfaces, shown to lead to reproducible switching from a metallic FM state to insulating AFM due to a reacted interface layer [2], magnetic anisotropy in the top layer [3], or to exchange-bias effects when Co was deposited on ferroelectric PZT [15]. Moreover, such a design, based on breaking the inversion symmetry in the contact region, activates interfacial Dzyaloshinskii-Moriya interactions between neighboring spins, which, competing with the Heisenberg collinear interaction, is the ingredient for stabilizing topologically protected magnetic phases such as interface skyrmions [14].

Here we grow an ultrathin, crystalline Ni layer on top of a ferroelectric $BaTiO_3$ (BTO) layer prepared in two distinct ferroelectric states through engineering of the growth sequence and demonstrate their radically different magnetic properties depending on the ferroelectric polarization of the substrate [16,17]. In ABO_3 perovskites, a layer-by-layer growth results in either AO- or BO_2-terminated surfaces. A common approach is the chemical etching of the substrate, frequently $SrTiO_3$ (STO) to TiO_2 termination in order to control the layer-by-layer sequence growth and propagate the BO_2 termination throughout the deposition process. Such a design strategy proved crucial considering the impact of the termination in systems hosting two-dimensional electron or hole gases (2DEG/2DHG) at polar interfaces ($LaAlO_3$/STO [18–21]) or for achieving control of the compensation mechanisms of ferroelectric films grown on STO [22].

In our case, the distinct ferroelectric states were stabilized by exploiting the different polarity [16,23] and work functions [24] of the MnO_2|BaO and LaSrO|TiO_2 sharp transition sequence at the interface of $La_{1-x}Sr_xMnO_3$ ($x = 0.3$) (LSMO) grown on TiO_2-terminated Nb-doped $SrTiO_3$ (STON) (001) with a ferroelectric BTO top layer. LSMO grown directly on STO propagates the BO_2 termination (MnO_2 in LSMO; TiO_2 in BTO), while $SrRuO_3$-buffered LSMO, due to Ru volatility, reverses the growth sequence to AO termination

*dana.popescu@infim.ro

(LaSrO in LSMO; BaO in BTO). The LSO termination in the contact region with BTO is positively charged, formally carrying $+0.7\,|e|$ (e is the elementary charge), while the MnO_2 is negatively charged, with $-0.7\,|e|$ per surface unit cell. The polar LaSrO termination, which carries positive charge, is essential in compensating the fixed ferroelectric (FE) charges in BTO, stabilizing a P- state (pointing from BTO towards LSMO), while the other sample is featured by P+ polarization (pointing in the opposite direction) [22].

We show in the following that when a thin 5-nm Ni film is deposited on BTO with the ferroelectric polarization pointing towards the top metal layer, the growth yields a smooth, well-oriented Ni(001) crystalline layer with robust ferromagnetism. For the opposite orientation of the ferroelectric layer, i.e., pointing towards the bottom LSMO layer, the Ni adlayer manifests a clear signature of coexisting FM and AFM phases, with the consequent exchange-bias interaction between the ferromagnetic Ni and the reacted NiO_x interface component.

II. SAMPLE PREPARATION, MATERIALS, AND METHODS

Ni deposition was performed on two oxide substrates prepared by pulsed laser deposition (PLD) : Ni/3.5 nm $BaTiO_3$/20 nm $La_xSr_{1-x}MnO_3$/Nb−$SrTiO_3$ ($x = 0.3$) denoted from now on as P1, and Ni/3.5 nm $BaTiO_3$/20 nm $La_xSr_{1-x}MnO_3$/5 nm $SrRuO_3$/ Nb−$SrTiO_3$ ($x = 0.3$) denoted throughout the text as P2. The multilayers were grown on STON substrates, Nb = 0.05% with (001) orientation using a KrF excimer laser (Lambda Physik COMPex205) with $\lambda = 248$ nm wavelength (from Surface GmbH). The STON substrates were treated chemically and thermally in order to achieve terraces with step height close to one single unit cell ∼0.4 nm [25–27]. Ceramic targets of $SrRuO_3$, $BaTiO_3$, and $La_{0.7}Sr_{0.3}MnO_3$ were used, and the layers were grown at 700 °C in different oxygen pressures (from 0.13 to 0.27 mbar).

The solid targets are ablated at laser fluencies of $2\,J/cm^2$ for SRO and LSMO and $1.5\,J/cm^2$ for BTO. Following the deposition, each layer (except for SRO) was annealed in 1 bar O_2 at the deposition temperature for 1 h in order to compensate for possible oxygen loss and creation of O vacancies. The samples were then transferred in the complex ultrahigh vacuum facility, including a molecular beam epitaxy (MBE) chamber equipped with *in situ* low-energy electron diffraction (LEED)-Auger capabilities and an x-ray photoelectron spectroscopy (XPS) chamber (by Specs). The base pressure of the MBE chamber is in the low 10^{-10} mbar range and that of the XPS chamber in the low-to-mid 10^{-9} mbar. The samples were then vacuum annealed at a temperature of 300 °C in order to remove most of the contaminants, resulting in a clean BTO surface (with carbon contamination less than one atomic layer).

Ni was deposited by MBE in UHV at a pressure $P \sim 2 \times 10^{-9}$ mbar on both oxide heterostructures, keeping the substrates at a temperature of 300 °C. The deposition was performed from a properly outgassed Knudsen cell at a rate of 1.0 ± 0.05 Å/min, as calibrated by a quartz thickness monitor.

There were two Ni deposition steps: one of 5 Å Ni (1.5 atomic layers, ML), in order to establish the growth picture in the early stages of the deposition process, and the second one of another 4.5 nm for a total thickness of the metallic overlayer equivalent to 5 nm Ni. Each step was followed by XPS measurements for the C 1*s*, O 1*s*, La 4*d*, Ba 3*d*, Mn 2*p*, Ti 2*p*, Ni 2*p* spectral regions.

XPS was performed in an analysis chamber equipped with a 150-mm hemispherical electron energy analyzer (Phoibos), a dual anode (Mg/Al $K\alpha$) x-ray source, and a monochromatized (Al $K\alpha$ /Ag $L\alpha$) x-ray source. Sample neutralization was achieved using a flood gun operating at 1-eV electron energy and 100-μA electron current. Only monochromatized Al $K\alpha$ radiation (1486.74 eV) was used in this experiment. The analyzer operated in fixed transmission (FAT) mode with pass energy of 20 eV; the estimated combined (source + analyzer) resolution is of about 0.75 ± 0.025 eV. The energy was calibrated using the C 1*s* core level for the C–C bond, at 284.6 eV.

Additional investigations by means of photoemission spectromicroscopy were performed with an AXIS Ultra DLD (Kratos Surface Analysis) setup operating in ultrahigh vacuum (10^{-9} mbar base pressure), equipped with a 165-mm hemispherical analyzer for spectroscopic measurements and spherical mirror analyzer for combined spectroscopy and imaging measurements. A monochromatized (Al Kα) x-ray source ($h\nu = 1486.74$ eV) was used. The spectromicroscopic mode uses the spherical mirror analyzer and the delay line detector to collect the spectroscopic signature of the Ni 2*p* core level from the top metallic layer and Ba 3*d* from the BTO substrate with a lateral resolution of 15 μm^2. The spectra in spectromicroscopic scans were acquired using field of view 2 (FOV2) mode, pass energy 160 eV, and apertures of 55 and 110 μm for individual and general spectra, respectively.

Characterization of surface morphology by means of atomic force microscopy and the distribution of the magnetic domain by using magnetic force microscopy (MFM) follows the *in situ* measurements. The total magnetization of the surface was characterized by magneto-optic Kerr effect (MOKE) [21,22].

The MFM measurements were performed on an Asylum MFP-3D atomic force microscope. The magnetic signal was mapped using a commercial CoCr-coated silicon cantilever with spring constant of 3.5 N/m and resonance frequency of 75 kHz. The magnetic information was recorded tracking the variation of the cantilever resonance induced by the magnetostatic force between the sample surface and magnetic tip.

Vector MOKE magnetometry measurements were performed in air, at room temperature, using a mini MOKE (AMACC Anderberg & Moder Accelerator AB) setup in a 90° geometry between the source and detector. The magnetic field was applied in both the sample and the incidence plane (longitudinal MOKE), with the laser beam ($h\nu = 640$ nm) at an incident angle of 45° with the sample plane. The polarizer and analyzer are of Glan-Thompson type, and the light modulation is achieved with a Faraday rotator (rodlike shape) working at 1000 Hz. The sample can be rotated in its own plane in order to change the direction of a possible magnetic anisotropy axis with respect to the direction of the applied field (azimuthal angle rotation). We performed measurements at three different azimuthal angles for each sample (0°, 45°, and 90°).

For structural characterization, x-ray diffraction (XRD) and x-ray reflection (XRR) measurements were performed *ex situ* using a Bruker-AXS D8 Advance system equipped with a copper target x-ray tube, nickel Kβ filter, and an x-ray mirror for incident beam parallelization. The measurements were performed in coplanar geometry with the horizontal sample stage so that the incident and the diffracted beams are always in-plane with the normal to the sample stage. The φ scans were performed by rotating the samples around the normal to the surface while keeping the goniometer arms in the Bragg condition for STON (103) and Ni (113) tilted planes.

First-principles calculations were performed within the density functional theory framework using the QUANTUM ESPRESSO code [28] by employing ultrasoft pseudopotentials [29] and the generalized gradient approximation functional in PBE parameterization of the exchange and correlation term. The code uses plane waves to expand the electronic wave function with explicit valence and semicore electrons. The generalized gradient approximation in the formulation of Perdew and Wang, GGA+U, is used to treat the correlation contribution and the exchange in the total Hamiltonian. For our system we employ 10-unit-cell ferroelectric slabs with two different FE polarization states, sandwiched between metallic LSMO and Ni electrodes. During the calculation, the coordinates of all atoms are allowed to relax along the z axis until the Hellman-Feynman forces on each atom are less than 50 meV/Å. A 40-Ry cutoff for the plane-wave expansion and 400 Ry for the charge-density integration is used. We were able to achieve convergence when relaxing the coordinates in the supercell for a $6 \times 6 \times 1k$-point mesh, while for a self-consistent electronic structure, a $10 \times 10 \times 1$–point mesh to sample the k space was used. The in-plane lattice constant of the heterostructure was fixed at the STON value, deduced from a previous bulk calculation to be $a = 3.936$ Å.

III. RESULTS AND DISCUSSION

We start by discussing the magnetic properties in direct connection with sample morphology for the two samples (Fig. 1). In Kerr effect magnetometry measurements, P1 is featured by symmetrical hysteresis loops with respect to the axis origin, indicating robust ferromagnetism [Fig. 1(a)]. Note that the rectangularity of the hysteresis loop is almost independent of the azimuthal angle and the ratio between remanence and saturation is much higher than 0.5, both features pointing therefore to no magnetic texture and magnetization reversal intermediated by magnetic wall displacements. The explanation for the progressive strong variation of the Kerr rotation angle at saturation with the azimuthal angle has an optical origin related to different scattering mechanisms of the incoming radiation on the films, depending on the growing characteristics of the top Ni film, as subsequently discussed. On the contrary, MOKE measurements on P2 reveal an almost constant amplitude of the Kerr rotation angle at saturation, independent of the measurement direction, while the MOKE hysteresis loop features clear shifts of 75–80 Oe (either positive or negative) with respect to the axis origin for different measurement directions [Fig. 2(b)]. Such behavior, with displacement of the MOKE loop along the x axis, accompanied by its asymmetric shape, points at an exchange-bias term due to some pinning mechanisms of the ferromagnetic phase by an antiferromagnetic component. The azimuth angles used for MOKE measurements are expressed with respect to the crystalline axes of the BTO substrate. The close resemblance of the MOKE curves of P2 recorded at 0° and 90°, and its different shape at 45°, suggest that the easy axis of the Ni is oriented at 45° with respect to the BTO ⟨110⟩ crystalline axis. For P1, no magnetic anisotropy is observed, indicating that there is no magnetic easy axis, or if one exists, it is contained within the Ni plane.

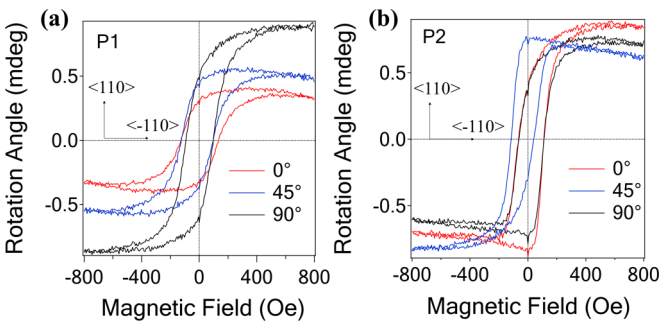

FIG. 1. Magnetization of the Ni|BTO surface resulting from MOKE measurements for (a) P1 and (b) P2 samples. The magnetization loops are acquired at different azimuthal angles with respect the BTO crystalline axes, as represented in the insets.

The striking similarities between AFM and MFM images (Figs. 2 and 3) with barely visible magnetic contrast in normal to plane direction gives an additional arguments for the expectation that due to the shape anisotropy [30–32] specific to such thin ferromagnetic films, all spins are oriented within the Ni overlayer plane. Thus, the relevant information on sample magnetism is encoded in our longitudinal MOKE measurements.

The question that arises now is whether the different magnetic response of the two samples originates or at least connects to their different growth morphology or involves electronic mechanisms only. The close resemblance of the AFM images, with terraces and similar stripe-shaped features (Fig. 2), to the MFM images for P1 and respectively grain-like morphology, homogeneously distributed over the whole surface of P2 (Fig. 3), suggests that the different magnetic properties of the two Ni films derive from a different growth mode, dependent on the polarization state of the bottom ferroelectric film [1,4,8,9,16,32], which in turn translates to different electronic properties. Moreover, one can exclude an initially different morphology of the oxide heterostructure surfaces (Fig. S1) as the BTO substrate for both P1 and P2 appear rather similar, with only atmosphere contaminants which were removed during the annealing in the preparation chamber (see Fig. S4).

Consequently, the crucial parameter that controls the particular growth mode of Ni connects to the ferroelectric state of the BTO in P1 and P2, resulting from the combination of different termination-engineered interfaces of BTO with LSMO [16,17] and of Ni with BTO and different work functions of P1 and P2 substrates [22,24].

In this sense, XPS measurements before and after Ni deposition confirm a distinct ferroelectric state of the BTO

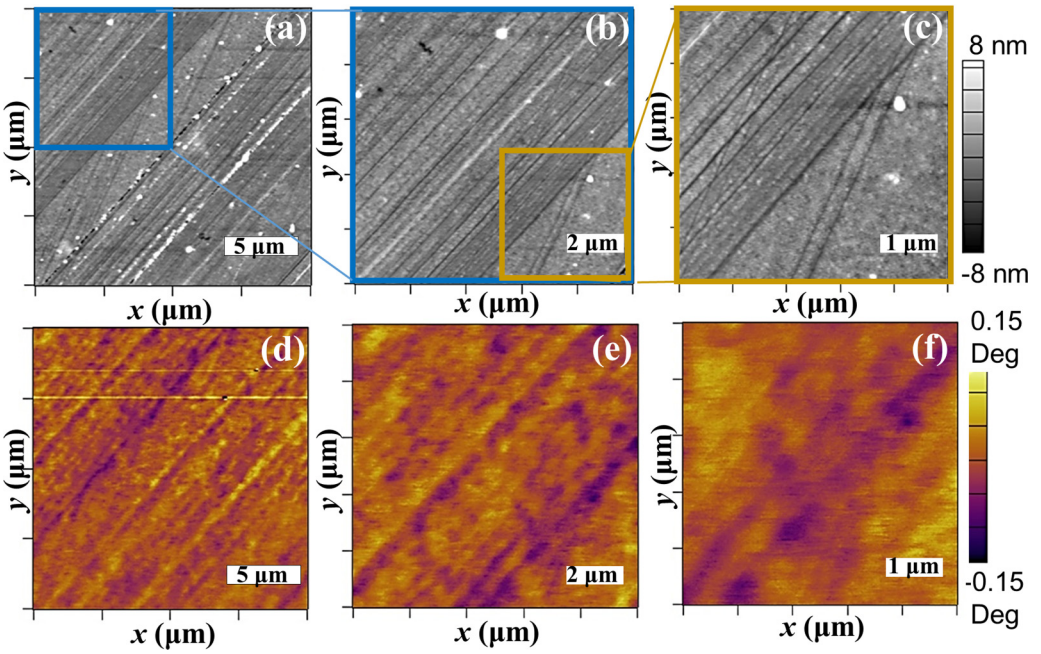

FIG. 2. Morphology and magnetic response derived from atomic force microscopy (a–c) and magnetic force microscopy (d–f) in representative regions of P1. Colored rectangles represent the corresponding zoomed-in areas, imaged by AFM and MFM.

through the relative shift of the binding energies of Ba $3d$, Ti $2p$, and O $1s$ core levels on P1 and P2, while giving an additional support for the different morphology of Ni grown on the oxide heterostructures.

Figure 4 shows the XPS spectra of Ni $2p$, Ba $3d$, O $1s$, and Ti $2p$ for the two studied samples. All spectra were simulated with Voigt profiles and associated inelastic backgrounds simulated by primitives of the Voigt function [33]. The O $1s$ spectrum has three components: the main peak at 529.3 eV (P1) and 528.7 eV (P2) associated with bulk BTO [34] and two other at higher binding energy corresponding to the surface contribution of oxygen in perovskite and residual C-O species at the surface. Ba $3d$ and Ti $2p$ were simulated with two components, accounting for bulk (lower binding energy BE) and surface (higher BE) contributions. Ni $2p$ was fitted with four components: the main one is the signature of metallic Ni, accompanied by a reacted NiO_x component at 1.2 eV higher BE, a Ni_2O_3 component at a BE ~3.2 eV away from the main metallic peak [35–38], and a small component at lower BEs, similar with the signature of strongly correlated

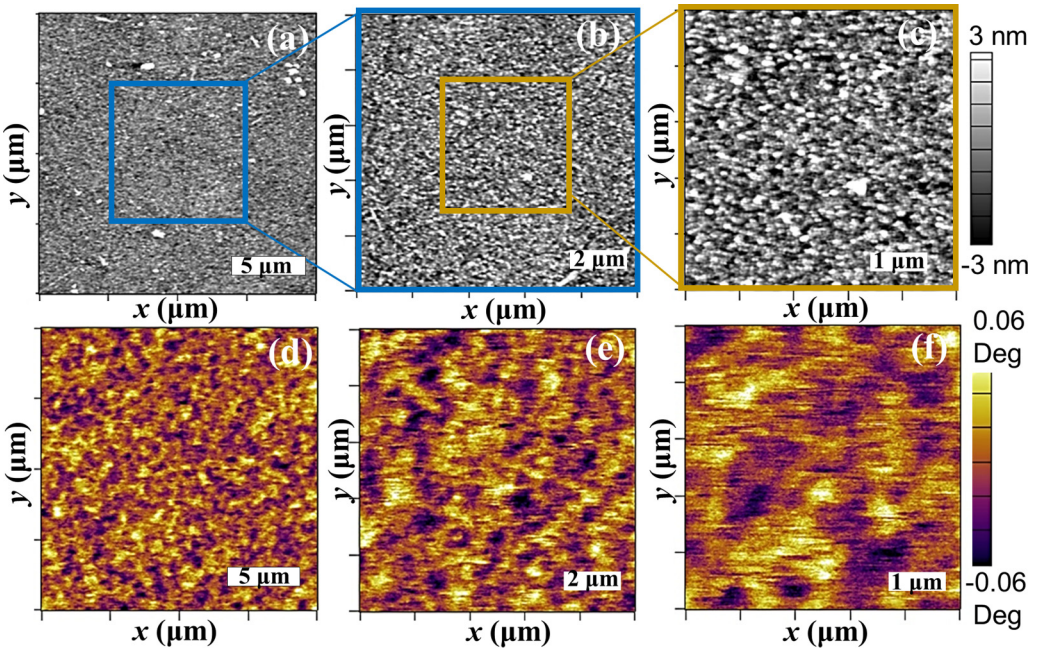

FIG. 3. Morphology and magnetic response derived from atomic force microscopy (a–c) and magnetic force microscopy (d–f) in representative regions of P2. Colored rectangles represent the corresponding zoomed-in areas, imaged by AFM and MFM.

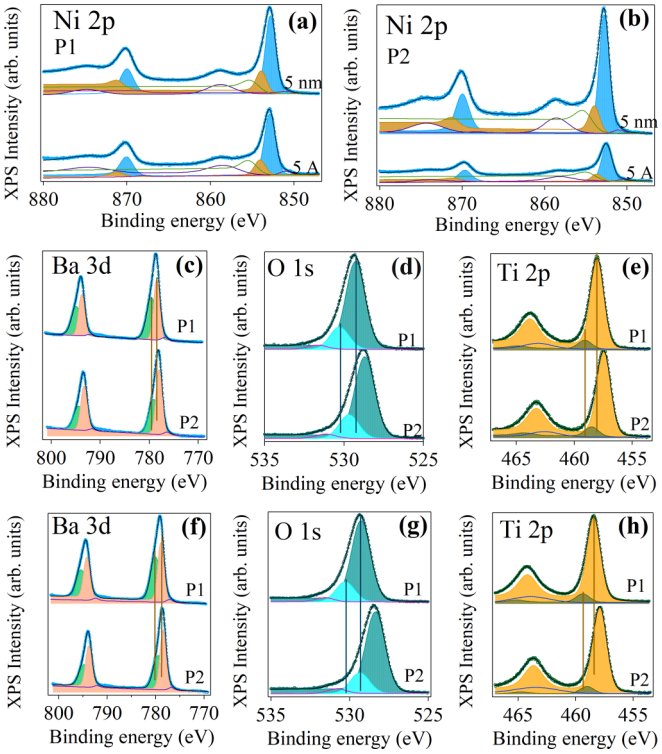

FIG. 4. Raw XPS spectra for P1 (a) and P2 (b) for two different Ni thicknesses. Filled blue component is the main Ni metallic line and yellow the NiO_x one. Single lines correspond respectively to correlated Ni (red), satellite (green), and Ni_2O_3 (violet). Comparison of BTO core levels for the clean P1 and P2 sample (c, d, e) and covered with 5 Å Ni (f, g, h). The vertical lines are used to better illustrate the difference of the binding energies. The blue markers represent the experimental data, the black line is the fit line. In (c) and (f), green components describe the surface, uncoordinated Ba atoms and the yellow one, the bulk signature of Ba in perovskite environment. In O 1*s* spectra (d, g), the filled dark green is the main perovskite-related component, cyan is the surface contribution of undercoordinated atoms, and the magenta line designates the oxygens from surface contaminants. In Ti 2*p* spectra (e, h), the light yellow filled component represents the main perovskite contribution, and the dark yellow corresponds to surface undercoordinated Ti atoms. The blue line is a satellite line.

Mn 2*p* electrons in LSMO [39]. As expected, the integral amplitudes of these smaller components at lower BEs decrease with increasing Ni thickness (and thus available electrons which screen the electron-electron interaction), confirming their correlated nature.

As clearly established in Refs. [22,40–47], the signature in photoemission of out-of-plane orientations of the ferroelectric polarization is given by the displacements towards higher or lower binding energies of both the valence band maxima and of the core levels for P+ or P− polarization state respectively. This derives from the particular alignment of the bands close to the surface or interface and the accompanying band bending, which accounts for the observed shifts [48]. The difference between the binding energies of the same core levels when the system lies in distinct out-of-plane polarization states is about 0.4–0.9 eV. In our case, relative shifts of ∼0.4–0.6 eV between the same core levels confirm

TABLE I. The main BTO surface signals in the XPS spectra for the clean samples with their statistical errors.

Electrons	Clean samples P1	P2
O 1*s*	64.8% ± 1.4%	63.1% ± 1.4%
Ti 2*p*	14.6% ± 0.7%	13.8% ± 0.7%
Ba 3*d*	13.7% ± 0.4%	15.1% ± 0.4%
La 4*d*	4.9% ± 1.2%	4.3% ± 1.2%
Mn 2*p*	2% ± 1.7%	3.7% ± 1.2%

that P1 lies in a P+ state, with the ferroelectric polarization oriented away from the surface, and P2 features P polarization, pointing towards the bottom interface with LSMO. Such results are in line with previous findings [16,17], where a SRO layer inserted between LSMO and STO substrate reverses the layer-by-layer growth sequence of the perovskite structures, modifies the work function of the substrate [24], and stabilizes a distinct polarization state compared with the case when no SRO buffer layer is inserted [22]. A confirmation of our growth strategy comes from inspecting the atomic concentrations of Ti and Ba for P1 and P2. One would expect that in case of P1, with all heterostructure deposited on the TiO_2 -terminated STON, the same termination (BO_2) would be in principle conserved through the growth process, while the reversed sequence (AO) would be associated with the SrO termination in SRO, which then propagates to LSMO (LaSrO) and BTO (BaO). Indeed, as seen in Table I, P1 features a higher Ti concentration and smaller Ba content, while the opposite situation arises for the P2 sample. Considering that Ti 2*p* and Ba 3*d* photoelectrons have similar probing depths d at their corresponding kinetic energies ($d \sim 3\lambda$, $\lambda_{Ba} = 12.46$ Å, and $\lambda_{Ti} = 15.81$ Å [47]), such variation corresponds exactly to the expected scenario, with P1 mostly TiO_2 terminated and in average, BaO termination for P2.

We stress that our macroscopic XPS measurements give only an averaged indication of the domain termination, as information is extracted from areas comparable with the size of the x-ray spot on the sample (which for our x-ray gun is of the order of mm^2). Additional photomicroscopy measurements performed with a lateral resolution of 15 μm^2 (see Appendix) seem to locally indicate, however, some coexistence of BO_2- and AO-terminated domains. Remarkably, even on the AO domains from the P1 sample, the FE polarization state remains P+, evident through the same shift towards higher BEs of Ba 3*d* and Ti 2*p* core levels, while the BO_2 domains of P2 are featured by the same P- FE state. This indicates that the major impact in stabilizing the FE polarization state is not of the termination but has to be connected to different work functions of the substrate [22,24]. Indeed, it was shown that insertion of an SRO buffer under LSMO decreases its work function with respect to the deposition on TiO_2-terminated STO [24], creating the prerequisite for a polarization state pointing towards the interface [22], while higher values of the substrate work function favor the stabilization of a ferroelectric polarization pointing away from the sample [22,41,43,46].

A second observation connects the intensity variations of the BTO buried under the Ni layer with the morphology observed in AFM. Comparing the attenuation of the surface

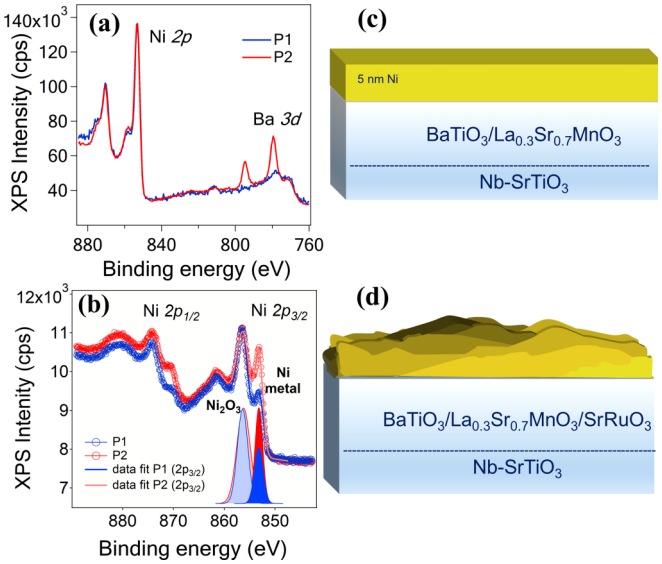

FIG. 5. XPS spectra on P1 and P2 samples immediately after deposition of 5 nm Ni (a) and post-MOKE measurements (b) along with the growth modes of Ni on both substrates (c and d).

peaks (Ba $3d$) caused by the thick Ni overlayer [Fig. 5(a)], it may seem surprising that the surface signatures of BTO manifest as if they are attenuated differently for the same thickness of the Ni overlayer (for details on additional x-ray reflectivity measurements, see Figs. S2b and S3 in the Supplemental Material [48]). However, the smaller attenuation in the case of P2 is in perfect agreement with the observed columnar morphology, with high roughness (∼0.8 nm) and "grains" separated by thinner Ni regions [Fig. 5(d)], which, due to weaker attenuation, still allow us to record some signal from the BTO underlayer. In the case of P1, stronger attenuation and a weaker signal from the BTO underlayer is compatible with the flat, continuous growth of Ni [Fig. 5(c)] and roughness smaller by a factor of 2, as established in AFM.

This raises in turn the concern of whether the antiferromagnetic signature identified in MOKE for P2 but not for P1 [Figs. 1(a) and 1(b)] may be related to the coexistence of metallic Ni and Ni in oxidized form; Ni_2O_3 resulted from partial oxidation of the metallic Ni during the *ex situ* magnetic measurements. One would naively expect that sample P2, with its higher roughness (and higher surface-to-volume ratio) would present a higher amount of oxidized Ni, which in turn would explain the presence of an antiferromagnetic signature in MOKE measurements. XPS-spectra-recorded post-MOKE measurements indicate that the opposite situation applies, namely, the ratio between the integral amplitudes of the metallic Ni $2p_{3/2}$ component and Ni_2O_3 is higher in the case of P2 than in P1 [Fig. 5(b)]. More exactly, the thickness of the oxide layer attenuating the signal from the metallic Ni, extracted from the ratio between the metal and oxide component amplitudes, is 3.5 nm Ni_2O_3 in the case of P1 and 2.3 nm for P2. Had the antiferromagnetic signature identified in MOKE originated in the coexisting metallic Ni and oxidized NiO component at the surface of the metallic layer, one should have seen at least a similar behavior for both samples. The fact that only P2 shows a signature of coexisting FM and AFM phases, while P1 manifests robust ferromagnetism with symmetrical magnetization reversal loops, indicates that the incidence of the AFM ordering and the consequent exchange bias observed in MOKE for P2 is independent of the oxidized surface layer. It suggests instead that their different behavior lies in the radically different interface nature of Ni grown on BTO with opposite ferroelectric orientations.

However, XRD measurements show that Ni deposited on both heterostructures grows as a (001) single oriented crystalline layer, with the same lattice constant $a_{Ni} = 3.519$ Å, as deduced from the corresponding Bragg angle, $2\theta = 51.92°$ [Fig. 4(a)], which is in perfect agreement with the bulk Ni fcc value.

Remarkably, the rocking curves (RCs) around the Ni(200) peaks feature FWHMs of 0.75° and 0.94° for P1 and P2, respectively, as deduced from the fit of the experimental data with two Voigt profiles. The sharp component describes the excellent out-of-plane orientation of the Ni single crystal and the broad one originates in the large dislocation densities within the Ni film. The sharp width is comparable with that of Ni single crystals [Fig. 6(c)] [49] or with that of perfectly epitaxial oxide structures prepared with atomic precision by PLD [50] and is an order of magnitude lower that Ni deposited on conventional semiconductors [51].

Moreover, the azimuth scans (φ scans) performed on tilted Ni (113) crystal planes reveal a fourfold symmetry and perfect overlap with that of the square surface unit cell of STON as derived from the scan on the STON (103) plane [Fig. 6(b)]. This indicates at a 45° rotated growth configuration of Ni with respect the oxide heterostructure unit cell, with the ideal epitaxial growth condition expressed as $a_{STON}\sqrt{2}/2 \cong d_{Ni-Ni}$ [Fig. 6(b)], with $a_{STON} = 3.907$ Å the STON substrate and $d_{Ni-Ni} = 2.488$ Å the interatomic distance between the Ni atoms.

Still, the significantly different lattice constant of Ni compared with the substrate is at odds with the remarkably well-ordered growth of Ni along the (001) surface suggested by the φ scans and RCs. Such contradicting behavior is reconciled by accepting that the formation of a thin NiO_x reacted layer acts as a buffer at the interface between Ni and BTO. Indeed, a thin enough NiO_x buffer layer, with the lattice constant not far from the theoretical 4.17 Å of NiO [52], could accommodate epitaxial strains of around 6% lattice mismatch with the substrate [53]. This would relieve the epitaxial strains between Ni and the substrate while initiating and stabilizing a well-defined growth direction. In our case there were bare similarities with previously reported oxygen scavenging from the substrate, involved in formation of a reacted interface layer [54]. Indeed, even if the small thickness of the reacted NiO_x interface component is beyond our XRD sensitivity, its appearance is confirmed in XPS measurements through the additional component accompanying the metallic peak at 1.2 eV higher binding energies (Fig. 4) in both P1 and P2 samples. Further details concerning the Ni layer and oxidized Ni thicknesses for P1 and P2 as deduced from x-ray reflectivity are presented in the Supplemental Material [48].

It is clear then that in order to solve the puzzle, an atomistic picture of the particular termination-controlled and ferroelectric-dependent Ni|BTO interface is required. We

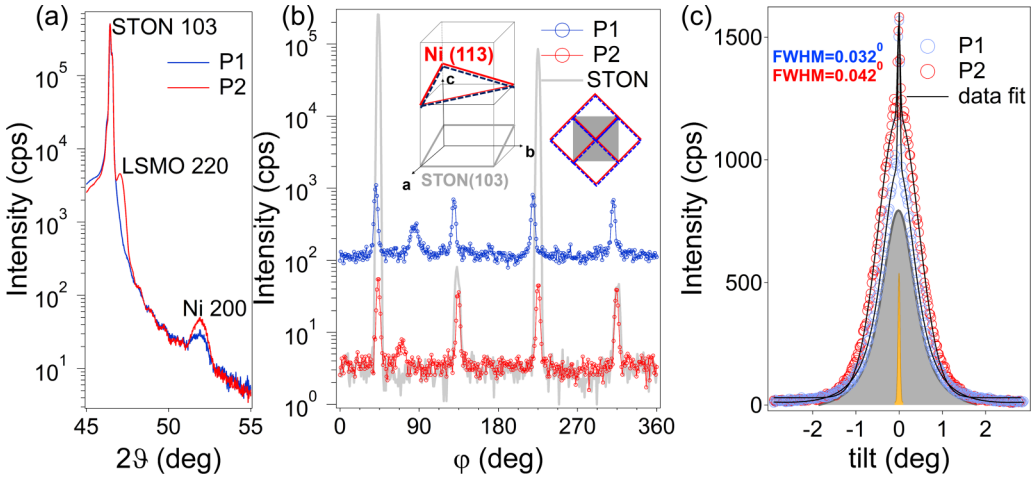

FIG. 6. (a) $2\theta - \omega$ XRD diagram of P1 and P2. (b) φ – scan on the STON (103) and Ni (113) planes. (c) Rocking curve around the 002 peak of Ni. Geometry of the (103) and (113) planes of STON and Ni, respectively, and the derived growth configuration of Ni on the oxide substrate are in the inset of (b).

establish it in first-principles calculations on two heterostructures constructed according to the information extracted from the XRD and XPS measurements, with in-plane parameters of the LSMO and BTO oxides perfectly matched at the STON in-plane lattice constant as indicated by the reciprocal space map (Fig. S2), and with different terminations for the P+ (TiO_2) and P- (BaO) states, as extracted from XPS analysis. In addition, we simulated the partial oxidation of the Ni interface layer through insertion of additional oxygen atoms, according to our previous assumption, supported by both diffraction and photoemission data.

The energetically most favorable relaxed structures are for Ni on BTO with ferroelectric polarization pointing towards the top metal (P+) in Fig. 7(a) and for Ni deposited on BTO with the opposite ferroelectric orientation in Fig. 7(b). Their corresponding spin-polarized charge-density isosurfaces and densities of states projected onto Ni 3d and Ti 3d-O 2p contributions indicate clearly that in the case of Ni deposited on BTO with P- state and BaO termination, the spins in the first three Ni interface layers close to the BTO contact region order antiferromagnetically with respect to the following Ni spins. On the other hand, when Ni grows on the BTO with the P+ state, the spins stay ferromagnetically ordered through the entire Ni slab, with only minor modulations of the magnetic moments. Table II summarizes the values of the calculated magnetic moments per Ni atom in each layer, starting from the interface and going towards the surface, where magnetic moments of both systems become essentially the same.

It is noteworthy that the formation energy, calculated as the difference between the energies of the LSMO|BTO|Ni system and of individual slabs in the same supercell, is 20 meV higher in the case of a P- state [Fig. 7(b)], indicating a slightly less favorable growth scenario compared with the growth on a P+ BTO surface. This supports the grainlike, columnar

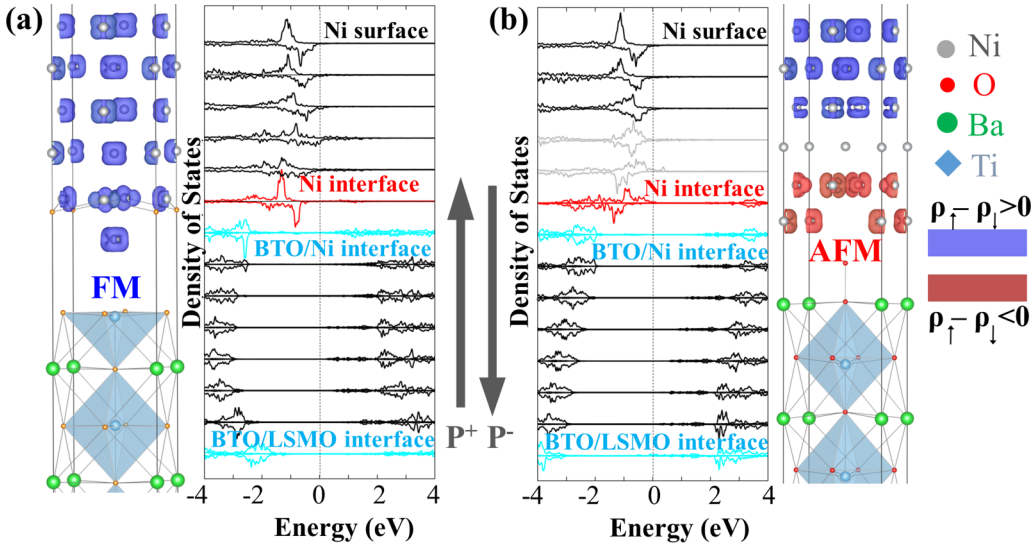

FIG. 7. Orbital-resolved O 2p-Ti 3d states in the BTO and Ni 3d DOS in the supercell for (a) P+ and (b) P− orientation of the ferroelectric layer. Spin-polarized charge densities with the isosurface of 0.1 $e/\text{Å}^3$ are shown in blue for positive values and red for negative.

TABLE II. Magnetic moments for the Ni atoms in the relaxed slab going from the interface (I) towards the surface.

	$M_I(\mu_B)$	$M_{I+1}(\mu_B)$	$M_{I+2}(\mu_B)$	$M_{I+3}(\mu_B)$	$M_{I+4}(\mu_B)$	$M_{I+5}(\mu_B)$
P1	0.67	0.60	0.55	0.63	0.64	0.70
P2	−0.77	−0.65	−0.12	0.46	0.64	0.69

growth on the P- surface as opposed to the smooth coverage on BTO in a P+ state and TiO_2 terminated. Moreover, the different FM-AFM coupling observed in MOKE at 0° and 45° (as resulting from the specific asymmetries and shifts of the loops) is stronger along the diagonal axis (Ni AFM coupled) than at 0 and 90°. This is, however, in perfect agreement with the model established in first-principles calculations for P2, as the orientation along the diagonal line should increase the coupling effect with the antiferromagnetic component by a factor of $\sqrt{2}$ (e.g., the ratio between antiferomagnetically oriented spins along the diagonal and along the median axis). Our results indicate an additional way to engineer the exchange-bias coupling and the asymmetrical magnetization reversal depending on the crystallographic orientation.

IV. CONCLUSIONS

Summarizing, our results show that depending on the out-of-plane polarization orientation of the ferroelectric BTO used as substrate, highly crystalline, textured Ni adlayers organize their growing characteristics in order to lead to larger or smaller magnetic domains with no magnetic texture and featured by a different coupling term of the ferromagnetic phase with the reacted interface antiferromagnetic phase. The essential ingredients in preparing the out-of-plane ferroelectric polarization are the proper engineering of the substrate work function and the layer-by-layer sequence growth of the ABO_3 perovskite heterostructures, with the BO_2 (TiO_2, MnO_2, TiO_2) termination stabilizing a ferroelectric polarization pointing from the bottom LSMO electrode to the top Ni metallic layer (P+). The AO termination (SrO, LaSrO, BaO), due to different polarity and work functions, favors the opposite orientation of the ferroelectric direction (P-), translating into different electronic properties of the metal/ferroelectric interface. As established by first-principles calculations, the reacted interface plays the key role in the observed antiferromagnetic phase stabilized at the interface with the ferroelectric in P- state, while the opposite direction features robust unpinned ferromagnetism. The current work aims to enlarge the perspective on metal/ferroelectric functionality, formulating a strategy to control the coexisting ferromagnetic and antiferromagnetic phases in metal/oxide interfaces for data storage and devices with direction-dependent exchange bias.

ACKNOWLEDGMENTS

This work was funded by the Ministry of Research and Innovation through Project No. PN-III-P4-ID-PCCF-2016-0047, granted through the UEFISCDI Agency, and by Project No. 18-ELI/2016, granted through the Institute of Atomic Physics. D.G.P. acknowledges partial funding from the PN-II-RU-TE-2014-4-1117.

APPENDIX: SPECTROMICROSCOPIC INVESTIGATIONS

Images in Fig. 8 were obtained by imaging the intensity ±1 eV around the Ni $2p_{3/2}$ peak, hence delimiting the Ni-covered region for P1 (a) and P2 (c) while the substrate was imagined by mapping the intensity ±1 eV around the Ba $3d_{5/2}$ peak in the region which during Ni deposition was covered by the metallic clamp. As Fig. 8 indicates, surfaces are rather homogenous, supporting the image derived from AFM investigations.

The evaluation of the integral amplitudes of spectra recorded in spectromicroscopic mode should in principle directly reflect the local composition. However, a precise description of local stoichiometry from spectromicroscopic individual scans is complicated by the contribution of the magnetic field of the spherical mirror analyzer, which modifies the trajectory of the photoelectrons and produces the modulations in intensity along the direction of the slit used to collect the signal. The slit regions are identified by the rectangles in Fig. S2 (a–d). Hence, termination effects of BTO substrate are probed through the Ni capping layer only. This allows us to collect the signal from the topmost region of BTO

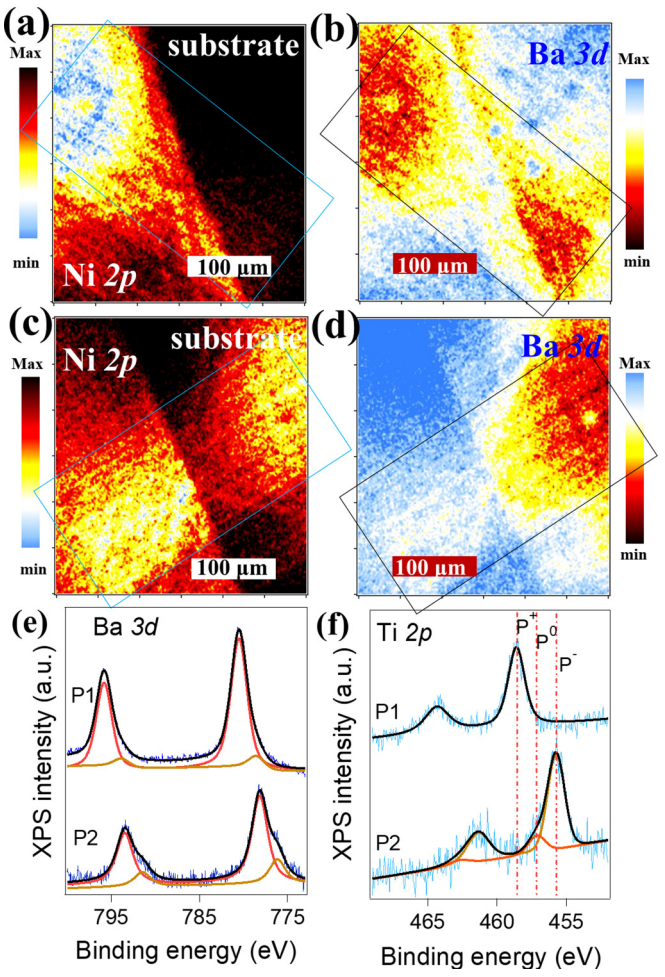

FIG. 8. Spectromicroscopic images of the metal-covered region obtained using Ni $2p_{3/2}$ peak for P1 (a) and P2 (c) and of the substrate using Ba $3d_{5/2}$ peak for P1 (b) and P2 (d). Ba $3d$ (e) and Ti $2p$ spectra recorded on P1 and P2 samples.

and suggests that, in addition to the overall TiO_2 termination of P1 and BaO termination for P2, one cannot completely exclude the scenario of regions having mixed BaO and TiO_2 terminations.

However, the ferroelectric character of P1 and P2 does not change, and in fact one can once more confirm clearly the different ferroelectric states of P1 and P2 extracted from their shifts towards lower binding energies (P−) or larger binding energies (P+). Moreover, the Ti $2p$ spectrum collected on P1 identifies a single polarization state, P+, while P2 is featured by mostly the P- state coexisting with regions with no out-of-plane ferroelectric polarization (P0), as indicated by the smaller component at higher binding energies.

[1] L. Bocher, A. Gloter, A. Crassous, V. Garcia, K. March, A. Zobelli, S. Valencia, S. Enouz-Vedrenne, X. Moya, N. D. Marthur, C. Deranlot, S. Fusil, K. Bouzehouane, M. Bibes, A. Barthélémy, C. Colliex, and O. Stéphan, Atomic and electronic structure of the $BaTiO_3$/Fe interface in multiferroic tunnel junctions, Nano Lett. **12**, 376 (2012).

[2] G. Radaelli, D. Petti, E. Plekhanov, I. Fina, P. Torelli, B. R. Salles, M. Cantoni, C. Rinaldi, D. Gutiérrez, G. Panaccione, M. Varela, S. Picozzi, J. Fontcuberta, and R. Bertacco, Electric control of magnetism at the Fe/$BaTiO_3$ interface, Nat. Commun. **5**, 3404 (2014).

[3] N. Jedrecy, H. J. von Bardeleben, V. Badjeck, D. Demaille, D. Stanescu, H. Magnan, and A. Barbier, Strong magnetoelectric coupling in multiferroic Co/$BaTiO_3$ thin films, Phys. Rev. B **88**, 121409(R) (2013).

[4] C. A. F. Vaz, J. Hoffman, Y. Segal, J. W. Reiner, R. D. Grober, Z. Zhang, C. H. Ahn, and F. J. Walker, Origin of the Magnetoelectric Coupling Effect in $Pb(Zr_{0.2}Ti_{0.8})PbO_3/La_{0.8}Sr_{0.2}MnO_3$ Multiferroic Heterostructures, Phys. Rev. Lett. **104**, 127202 (2010).

[5] Y. Sun, Y. Ba, A. Chen, W. He, W. Wang, X. Zheng, L. Zou, Y. Zhang, Q. Yang, L. Yan, C. Feng, Q. Zhang, J. Cai, W. Wu, M. Liu, L. Gu, Z. Cheng, C.-W. Nan, Z. Qiu, Y. Wu, J. Li, and Y. Zhao, Electric-field modulation of interface magnetic anisotropy and spin reorientation transition in $(Co/Pt)_3$/PMN−PT heterostructure, ACS Appl. Mater. Interfaces **9**, 10855 (2017).

[6] R. Cai and A. M. Jonas, Local maps of the polarization and depolarization in organic ferroelectric field-effect transistors, Sci. Rep. **6**, 22116 (2016).

[7] Y. W. Yin, J. D. Burton, Y.-M. Kim, A. Y. Borisevich, S. J. Pennycook, S. M. Yang, T. W. Noh, A. Gruverman, X. G. Li, E. Y. Tsymbal, and Q. Li, Enhanced tunnelling electroresistance effect due to a ferroelectrically induced phase transition at a magnetic complex oxide interface, Nat. Mater. **12**, 397 (2013).

[8] C.-G. Duan, S. S. Jaswal, and E. Y. Tsymbal, Predicted Magnetoelectric Effect in Fe/BaTiO Multilayers: Ferroelectric Control of Magnetism, Phys. Rev. Lett. **97**, 047201 (2006).

[9] B. Cui, C. Song, F. Li, X. Y. Zhong, Z. C. Wang, P. Werner, Y. D. Gu, H. Q. Wu, M. S. Saleem, S. S. P. Parkin, and F. Pan, Electric-Field Control of Oxygen Vacancies and Magnetic Phase Transition in a Cobaltite/Manganite Bilayer, Phys. Rev. Appl. **8**, 044007 (2017).

[10] H. Chen, Q. Qiao, M. S. J. Marshall, A. B. Georgescu, A. Gulec, P. J. Phillips, R. F. Klie, F. J. Walker, C. H. Ahn, and S. Ismail-Beigi, Reversible modulation of orbital occupations via an interface-induced polar state in metallic manganites, Nano Lett. **14**, 4965 (2014).

[11] D. Preziosi, M. Alexe, D. Hesse, and M. Salluzzo, Electric-Field Control of the Orbital Occupancy and Magnetic Moment of a Transition-Metal Oxide, Phys. Rev. Lett **115**, 157401 (2015).

[12] J. Li, A. Tan, K. W. Moon, A. Doran, M. A. Marcus, A. T. Young, E. Arenholz, S. Ma, R. F. Yang, C. Hwang, and Z. Q. Qiu, Tailoring the topology of an artificial magnetic skyrmion, Nat. Commun. **5**, 4704 (2014).

[13] A. Hrabec, J. Sampaio, M. Belmeguenai, I. Gross, R. Weil, S. M. Chérif, A. Stashkevich, V. Jacques, A. Thiaville, and S. Rohart, Current-induced skyrmion generation and dynamics in symmetric bilayers, Nat. Commun. **8**, 15765 (2017).

[14] S. Woo, K. Litzius, B. Krüger, M.-Y. Im, L. Caretta, K. Richter, M. Mann, A. Krone, R. M. Reeve, M. Weigand, P. Agrawal, I. Lemesh, M.-A. Mawass, P. Fischer, M. Kläui, and G. S. D. Beach, Observation of room-temperature magnetic skyrmions and their current-driven dynamics in ultrathin metallic ferromagnets, Nat. Mater. **15**, 501 (2016).

[15] A. Quindeau, I. Fina, X. Marti, G. Apachitei, P. Ferrer, C. Nicklin, E. Pippel, D. Hesse, and M. Alexe, Four-state ferroelectric spin-valve, Sci. Rep. **5**, 9749 (2015).

[16] P. Yu, W. Luo, D. Yi, J. X. Zhang, M. D. Rossell, C.-H. Yang, L. You, G. Singh-Bhalla, S. Y. Yang, Q. He, Q. M. Ramasse, R. Erni, L. W. Martin, Y. H. Chu, S. T. Pantelides, S. J. Pennycook, and R. Ramesh, Interface control of bulk ferroelectric polarization, PNAS **109**, 9710 (2012).

[17] G. de Luca, N. Strkalj, S. Manz, C. Bouillet, M. Fiebig, and M. Trassin, Nanoscale design of polarization in ultrathin ferroelectric heterostructures, Nat. Commun. **8**, 1419 (2017).

[18] A. Ohtomo and H. Y. Hwang, A high-mobility electron gas at the $LaAlO_3/SrTiO_3$ heterointerface, Nature (London) **427**, 423 (2004).

[19] M. Huijben, G. Rijnders, D. H. A. Blank, S. Bals, S. van Aert, J. Verbeeck, G. van Tendeloo, A. Brinkman, and H. Hilgenkamp, Electronically coupled complementary interfaces between perovskite band insulators, Nat. Mater. **5**, 556 (2006).

[20] H. Lee, N. Campbell, J. Lee, T. J. Asel, T. R. Paudel, H. Zhou, J. W. Lee, B. Noesges, J. Seo, B. Park, L. J. Brillson, S. H. Oh, E. Y. Tsymbal, M. S. Rzchowski, and C. B. Eom, Direct observation of a two-dimensional hole gas at oxide interfaces, Nat. Mater. **17**, 231 (2018).

[21] K. J. Kormondy, L. Gao, X. Li, S. Lu, A. B. Posadas, S. Shen, M. Tsoi, M. R. McCartney, D. J. Smith, J. Zhou, L. L. Lev, M. A. Husanu, V. N. Strocov, and A. A. Demkov, Large positive linear magnetoresistance in the two-dimensional t_{2g} electron gas at the $EuO/SrTiO_3$ interface, Sci. Rep. **8**, 7721 (2018).

[22] L. C. Tănase, L. E. Abramiuc, D. G. Popescu, A.-M. Trandafir, N. G. Apostol, I. C. Bucur, L. Hrib, L. Pintilie, I. Pasuk, L. Trupină, and C. M. Teodorescu, Polarization Orientation in

Lead Zirconate Titanate (001) Thin Films Driven by the Interface with the Substrate, Phys. Rev. Appl. **10**, 034020 (2018).

[23] S. Koohfar, A. S. Disa, M. S. J. Marshall, F. J. Walker, C. H. Ahn, and D. P. Kumah, Structural distortions at polar manganite interfaces, Phys. Rev. B **96**, 024108 (2017).

[24] M. Minohara, R. Yasuhara, H. Kumigashira, and M. Oshima, Termination layer dependence of Schottky barrier height for $La_{0.6}Sr_{0.4}MnO_3/Nb:SrTiO_3$ heterojunctions, Phys. Rev. B **81**, 235322 (2010).

[25] W. Saenrang, B. A. Davidson, F. Maccherozzi, J. P. Podkaminer, J. Irwin, R. D. Johnson, J. Freeland, J. Íñiguez, J. L. Schad, K. Reierson, J. C. Frederick, C. A. F. Vaz, L. Howald, T. H. Kim, S. Ryu, M. v. Veenendaal, P. G. Radaelli, S. S. Dhesi, M. S. Rzchowski, and C. B. Eom, Deterministic and robust room-temperature exchange coupling in monodomain multiferroic $BiFeO_3$ heterostructures, Nat. Commun. **8**, 1583 (2017).

[26] A. G. Boni, C. F. Chirila, R. Negrea, C. Ghica, I. Pasuk, I. Pintilie, and L. Pintilie, *Electrical Properties of Epitaxial Ferroelectric Heterostructures in Epitaxy*, edited by M. Zhong (Intech Open, London, 2018).

[27] W. Hong, H. N. Lee, M. Yoon, H. M. Christen, D. H. Lowndes, Z. Suo, and Z. Zhang, Persistent Step-Flow Growth of Strained Films on Vicinal Substrates, Phys. Rev. Lett. **95**, 095501 (2005).

[28] P. Gianozzi, S. Baroni, N. Bonini, M. Calandra, R. Car, C. Cavazzoni, D. Ceresoli, G. L. Chiarotti, M. Cococcioni, I. Dabo, A. Dal Corso, S. de Gironcoli, S. Fabris, G. Fratesi, R. Gebauer, U. Gerstmann, C. Gougoussis, A. Kokalj, M. Lazzeri, L. Martin-Samos *et al.*, QUANTUM ESPRESSO: a modular and open-source software project for quantum simulations of materials, J. Phys. C **21**, 395502 (2009).

[29] K. F. Garrity, J. W. Bennett, K. M. Rabe, and D. Vanderbilt, Pseudopotentials for high-throughput DFT calculations, Comput. Mater. Sci. **81**, 446 (2014).

[30] N. G. Gheorghe, M. A. Husanu, G. A. Lungu, R. M. Costescu, D. Macovei, D. G. Popescu, and C. M. Teodorescu, Reactivity, magnetism and local atomic structure in ferromagnetic Fe layers deposited on Si(001), Dig. J. Nanomater. Biostruct. **7**, 373 (2012).

[31] G. A. Lungu, N. G. Apostol, L. E. Stoflea, R. M. Costescu, D. G. Popescu, and C. M. Teodorescu, Room temperature ferromagnetic, anisotropic, germanium rich FeGe(001) alloys, Materials **6**, 612 (2013).

[32] J. D. Burton and E. Y. Tsymbal, Prediction of electrically induced magnetic reconstruction at the manganite/ferroelectric interface, Phys. Rev. B **80**, 174406 (2009).

[33] C. M. Teodorescu, J. M. Esteva, R. C. Karnatak, and A. El Afif, An approximation of the Voigt I profile for the fitting of experimental X-ray absorption data, Nucl. Instrum. Methods Phys. Res., Sect. A **345**, 141 (1994).

[34] D. G. Popescu, N. Barrett, C. Chirila, I. Pasuk, and M. A. Husanu, Influence of hole depletion and depolarizing field on the $BaTiO_3/La_{0.6}Sr_{0.4}MnO_3$ interface electronic structure revealed by photoelectron spectroscopy and first-principles calculations, Phys. Rev. B **92**, 235442 (2015).

[35] A. N. Mansour, Gold Mg Kα XPS spectra from the physical electronics model 5400 spectrometer, Surf. Sci. Spectra **3**, 211 (1994).

[36] Y. R. Lin, Y. S. Liao, H. T. Hsiao, and C. P. Chen, Photocatalytic hydrogen generation from raw water using zeolite/polyaniline@Ni_2O_3 nanocomposite as a novel photoelectrode, Appl. Surf. Sci. **504**, 144478 (2020).

[37] I. Preda, A. Gutiérrez, M. Abbate, F. Yubero, J. Méndez, and L. Alvarez, Interface effects in the Ni $2p$ x-ray photoelectron spectra of NiO thin films grown on oxide substrates, Phys. Rev. B **77**, 075411 (2008).

[38] G. Zhao, H. Hu, W. Chen, Z. Jiang, S. Zhang, J. Huang, and Y. Lu, $Ni_2O_3-Au^+$ hybrid active sites on NiO_x@Au ensembles for low-temperature gas-phase oxidation of alcohols, Catal. Sci. Technol. **3**, 404 (2013).

[39] K. Horiba, M. Taguchi, A. Chainani, Y. Takata, E. Ikenaga, D. Miwa, Y. Nishino, K. Tamasaku, M. Awaji, A. Takeuchi, M. Yabashi, H. Namatame, M. Taniguchi, H. Kumigashira, M. Oshima, M. Lippmaa, M. Kawasaki, H. Koinuma, K. Kobayashi, T. Ishikawa, and S. Shin, Nature of the Well Screened State in Hard X-Ray Mn $2p$ Core-Level Photoemission Measurements of $La_{1-x}Sr_xMnO_3$ Films, Phys. Rev. Lett. **93**, 236401 (2004).

[40] N. G. Apostol, L. E. Stoflea, G. A. Lungu, C. Chirila, L. Trupina, R. F. Negrea, C. Ghica, L. Pintilie, and C. M. Teodorescu, Charge transfer and band bending at $Au/Pb(Zr_{0.2}Ti_{0.8})O_3$ interfaces investigated by photoelectron spectroscopy, Appl. Surf. Sci. **273**, 415 (2013).

[41] N. G. Apostol, L. E. Stoflea, G. A. Lungu, C. A. Tache, D. G. Popescu, L. Pintilie, and C. M. Teodorescu, Band bending at free $Pb(Zr, Ti)O_3$ surfaces analyzed by X-ray photoelectron spectroscopy, Mater. Sci. Eng., B **178**, 1317 (2013).

[42] E. Kroger, A. Petraru, A. Quer, R. Soni, M. Kallane, N. A. Pertsev, H. Kohlstedt, and K. Rossnagel, *In situ* hard x-ray photoemission spectroscopy of barrier-height control at metal/PMN-PT interfaces, Phys. Rev. B **93**, 235415 (2016).

[43] L. Pintilie, C. Ghica, C. M. Teodorescu, I. Pintilie, C. Chirila, I. Pasuk, L. Trupina, L. Hrib, A. G. Boni, N. G. Apostol, L. E. Abramiuc, R. Negrea, M. Stefan, and D. Ghica, Polarization induced self-doping in epitaxial $Pb(Zr_{0.2}Ti_{0.8})O_3$ thin films, Sci. Rep. **5**, 14974 (2015).

[44] I. Pintilie, C. M. Teodorescu, C. Ghica, C. Chirila, A. G. Boni, L. Hrib, I. Pasuk, R. Negrea, N. G. Apostol, and L. Pintilie, Polarization-control of the potential barrier at the electrode interfaces in epitaxial ferroelectric thin films, ACS Appl. Mater. Interfaces **6**, 2929 (2014).

[45] D. G. Popescu, M. A. Husanu, C. Chirila, L. Pintilie, and C. M. Teodorescu, The interplay of work function and polarization state at the Schottky barriers height for $Cu/BaTiO_3$ interface, Appl. Surf. Sci. **502**, 144101 (2019).

[46] D. G. Popescu, M. A. Husanu, C. Chirila, L. Pintilie, and C. M. Teodorescu, Impact on ferroelectricity and band alignment of gradually grown Au on $BaTiO_3$, Phys. Status Solidi – RRL **13**, 1900077 (2019).

[47] N. G. Apostol and C. M. Teodorescu, Band bending at metal-semiconductor interfaces, ferroelectric surfaces and metal-ferroelectric interfaces investigated by photoelectron spectroscopy, in *Surface Science Tools for Nanomaterials Characterization*, edited by C. S. S. R. Kumar (Springer, Berlin, 2015).

[48] See Supplemental Material at http://link.aps.org/supplemental/10.1103/PhysRevMaterials.4.034402 for additional information on atomic force microscopy investigations, x-ray

reflectivity, reciprocal space mapping and initial stoichiometry from x-ray photoelectron spectroscopy.

[49] J. W. Shin, A. Standley, and E. Chason, Epitaxial electrodeposition of freestanding large area single crystal substrate, Appl. Phys. Lett. **90**, 261909 (2007).

[50] C. Chirila, A. G. Boni, I. Pasuk, R. Negrea, L. Trupina, G. Le Rhun, S. Yin, B. Vilquin, I. Pintilie, and L. Pintilie, Comparison between the ferroelectric/electric properties of the $PbZr_{0.52}Ti_{0.48}O_3$ films grown on Si (100) and on STO (100) substrates, J. Mater. Sci. **50**, 3883 (2015).

[51] A. E. Bocirnea, R. M. Costescu, I. Pasuk, G. A. Lungu, and C. M. Teodorescu, Band bending at magnetic Ni/Ge(001) interface investigated by X-ray photoelectron spectroscopy, Appl. Surf. Sci. **424**, 337 (2017).

[52] M. Baumer, D. Cappus, H. Kuhlenbeck, H.-J. Freund, G. Wilhelmi, A. Brodde, and H. Neddermeyer, The structure of thin NiO(100) films grown on Ni(100) as determined by low-energy-electron diffraction and scanning tunneling microscopy, Surf. Sci. **253**, 116 (1991).

[53] L. Wang, Z. Zeng, W. Gao, T. Maxson, D. Raciti, M. Giroux, X. Pan, C. Wang, and J. Greeley, Tunable intrinsic strain in two-dimensional transition metal electrocatalysts, Science **363**, 870 (2019).

[54] A. B. Posadas, K. J. Kormodny, W. Guo, P. Ponath, J. Geler-Kremer, T. Hadamek, and A. A. Demkov, Scavenging of oxygen from $SrTiO_3$ during oxide thin film deposition and the formation of interfacial 2DEGs, J. Appl. Phys. **121**, 105302 (2017).